



Contents lists available at ScienceDirect

Journal of the Mechanics and Physics of Solids

journal homepage: www.elsevier.com/locate/jmps

Quantitative surface topography of martensitic microstructure by differential interference contrast microscopy

Zhuohui Zeng^a, Chenbo Zhang^a, Shengwang Du^b, Xian Chen^{a,*}

^aDepartment of Mechanical and Aerospace Engineering, Hong Kong University of Science and Technology, Hong Kong

^bDepartment of Physics, Hong Kong University of Science and Technology, Hong Kong

ARTICLE INFO

Article history:

Received 19 August 2018

Revised 4 October 2018

Accepted 4 October 2018

Available online 10 October 2018

Keywords:

Differential interference contrast
Surface topographic characterization
Optical path gradient
Martensitic microstructure

ABSTRACT

We theorize a mathematical model by which the topography and the full-field deformation of martensitic microstructure are quantitatively determined by the reflected light differential interference contrast microscopy technique. Using the commercial reflected light DIC microscope (Nikon Ni-U), we determine the optical parameters for the proposed mathematical model using calibrated standard samples. Based on the theory, we conduct an experiment to demonstrate the determination of the surface relief of the microstructure comprised of a pair of twinned martensitic variants. The surface height gradients of the two martensite variants along the beam-shear direction of DIC agree well with the values measured by the atomic force microscopy. The measured results of twin laminates reveal that the current microscopy system can resolve the microstructure with the fineness of around 500 nm. Compared with the AFM results, it measures the surface slope with 0.005 rad accuracy. This paper underlies a new approach for quantitative surface topography determination with wide applications in experimental mechanics.

© 2018 Elsevier Ltd. All rights reserved.

1. Introduction

In crystalline solids, the formation of complex microstructures during reversible phase transformation has a significant impact on the functional fatigue properties and some transport properties of the materials such as the recoverable transformation strains, temperature dependent polarization and magnetization. The recent developments of phase-transforming materials show that the functionalities of such materials strongly rely on the modes of deformation and the conditions of elastic compatibility at phase boundaries. For example, the rate capability of olivine-type lithium batteries strongly depends on the strain accommodation during the charging/discharging procedure (Meethong et al., 2007). Another example is the ferromagnetic Heusler alloys with wide applications in sensing, actuation and magnetic refrigeration. By far, many examples show that the large jump of magnetization and caloric performance in cyclic transformations are closely related to the elastic compatibility conditions between the ferromagnetic and nonferromagnetic phases (Bhatti et al., 2012; Li et al., 2018; Srivastava et al., 2010; 2011; Zhao et al., 2017).

Particularly for martensitic materials, the macroscopic properties such as thermal hysteresis and degradation of pseudoelasticity over the cyclic thermal/stress-induced transformations have been theoretically proven to be linked to the following

* Corresponding author.

E-mail address: xianchen@ust.hk (X. Chen).

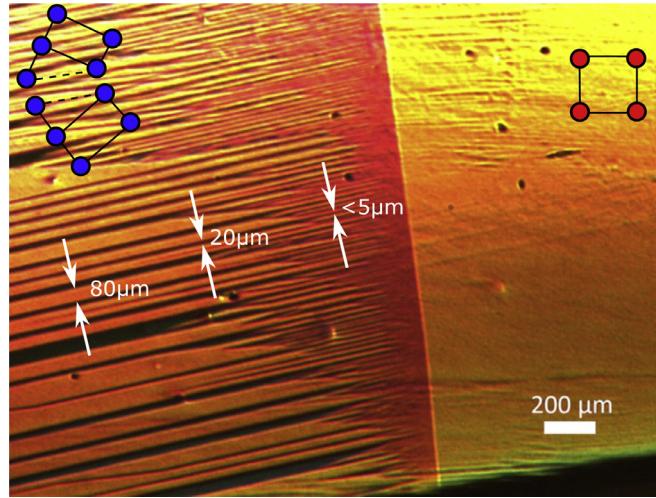


Fig. 1. A typical martensitic microstructure consisting of laminated twins branching into austenite through an elastic transition layer in single crystal Ni_2MnGa .

conditions (Chen et al., 2013; Zhang et al., 2009)

$$\lambda_2(\mathbf{U}) = 1, \quad (1a)$$

$$(\mathbf{a} \cdot \mathbf{v}_2(\mathbf{U}))(\mathbf{n} \cdot \mathbf{v}_2(\mathbf{U})) = 0. \quad (1b)$$

$$\text{tr}\mathbf{U}^2 - \det\mathbf{U}^2 - \frac{|\mathbf{a}|^2|\mathbf{n}|^2}{4} - 2 \geq 0. \quad (1c)$$

Here $\mathbf{U} \in \mathbb{R}^{3 \times 3}$ is the transformation stretch tensor (Chen et al., 2016a) underlying the symmetry-breaking martensitic phase transformation. The positive real number λ_2 is the middle eigenvalue of the stretch tensor \mathbf{U} corresponding to the normalized eigenvector \mathbf{v}_2 . The real vectors \mathbf{a} and \mathbf{n} are the twin parameters determined by the crystallography theory of martensite (Ball and James, 1987). When these conditions are satisfied by special lattice parameters of austenite and martensite, the thermal hysteresis is minimized. At the same time the phase reversibility, exhibited as the migration of latent heat/transition temperature and the degradation of pseudoelasticity, can be enhanced. A plethora of experiments (Chen et al., 2013; Chluba et al., 2015; Cui et al., 2006; James and Zhang, 2005; Ni et al., 2016; Song et al., 2013; Zarnetta et al., 2010) were conducted in a wide variety of martensitic materials, which conclusively confirm such relationships not only for the bulk materials, but also for thin films and micro-scale structures.

Geometrically, the conditions of (1a)–(1c) determine the formation of martensitic microstructures and the morphological configurations of compatible austenite/martensite interfaces (Chen et al., 2013) without elastic transition layer. Physically, these conditions guide the development for materials with ultra-low functional fatigue properties (Chluba et al., 2015; Song et al., 2013). An important step during such theory-based material development is the examination of martensitic microstructures quantitatively, since the morphological configurations of microstructure is the most straightforward way of identifying the compatibility of the interfaces. Here, “quantitatively” refers to (1) the morphological configurations of martensite; (2) the full-field deformation gradients responsible for the structural phase transformation; (3) the martensite variant assignment and interface normals. An essential feature of the morphology of the martensitic microstructure in these materials is that the surface reliefs of the martensite after the phase transformation contains the important crystallographic information associated with finite piecewise transformation strains. In Fig. 1, we show a typical martensitic microstructure in single crystal Ni_2MnGa undergoing martensitic transformation from cubic to tetragonal. The laminated twins of two martensite variants (left) meet up with the uniform austenite (right) through a transition layer. It is clear that neither of the martensite variants can solely form compatible interface with austenite due to the lack of compatibility, which indicates that this material, at least, does not satisfy the condition (1a). But it is still unclear how much strain there are in the elastic transition layer and how we understand these martensitic microstructures quantitatively.

Fig. 1 also underlies the morphological scale range of austenite and martensite. The twin width gets finer and finer as approaching to the austenite and martensite interface, of which the scale spans a wide range from hundreds of nano meters to tens of microns. In order to capture the morphological properties with quantitative analysis for both interface and the twin laminate, the optical techniques are very suitable.

The optical interferential techniques such as Moiré analysis and holography have been widely applied to experimental mechanics for determination of surface strain fields (Durelli and Parks, 1970; Zhang et al., 2000), but it is difficult to observe

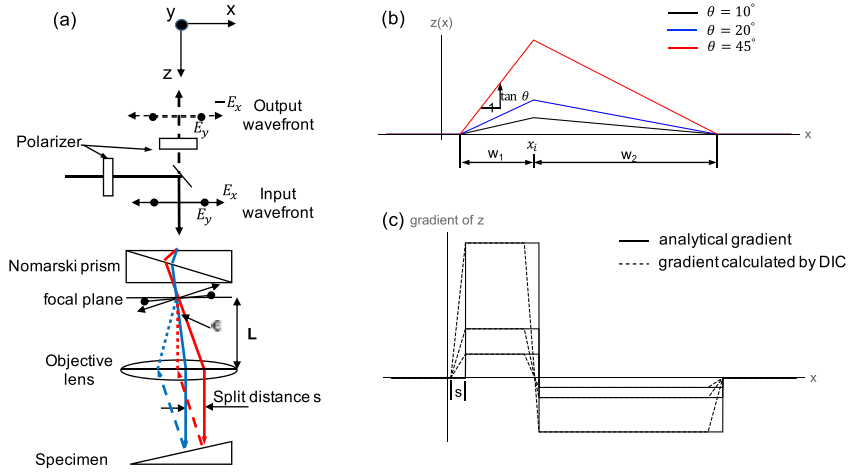


Fig. 2. (a) Optical path and wavefront relationships of the Nikon Ni-U reflected light DIC microscope. (b) Various surface topographies along x -axis with the slopes at angles of 10° , 20° and 45° ; (c) The surface height gradients of (b). (For interpretation of the references to color in this figure, the reader is referred to the web version of this article.)

the microstructure simultaneously during the measurement due to the surface gratings. The distortion-corrected digital image correlation is a widely used optical method for determination of in-plane deformation (Peters and Ranson, 1982). With the development of fast image processing algorithms, this has become the most popular modern experimental mechanics method for surface strain characterization. Utilizing the scanning electron microscopy, the digital image correlation method provides sub-grain size strain measurement with nanometer spatial resolution (Kimiecik et al., 2016). It has been applied to the study of the cyclic stress-induced phase transformation in NiTi shape memory alloy. However, these methods require high quality speckle patterns on top of the sample surface, which may block the geometric nature of the microstructures.

Reflected light differential interference contrast (DIC) microscopy is usually used to observe microstructures in opaque materials (de Groot, 2015; Nomarski, 1952), in particular in martensitic materials for its high contrast between the twin laminates (Heczko et al., 2013). But it lacks the quantitative information of the surface topography. In this paper, we theorize a mathematical model for the reflected light DIC module, by which both topography and surface height gradients are simultaneously and quantitatively determined. Combined with the crystallography analysis of martensite, we utilized the results from the DIC measurement to assign the martensitic variant in each of the martensite sub-domains, and further determine the full-field deformation map.

2. Principle and theoretical frame of the method

The optical path of our microscope (Nikon Ni-U reflected light DIC microscope) is shown in Fig. 2(a). Emitted from the halogen source and filtered by a polarizer, the light becomes a linearly polarized beam with orthogonal polarization components $|E_x| = |E_y|$, i.e. polarized along 45° from x -axis. After passing through a Nomarski DIC prism (NP), the linear rays with polarization E_x are spatially sheared along x -axis with an angle ϵ , i.e. the red light beam in Fig. 2(a). When the two beams arrive at the specimen surface, a spatial distance $s = f\epsilon$ is gained, in which f is the focal length of the objective lens of the microscope. Due to the birefringence effect of the prism, a phase lag is generated between E_x and E_y . After passing through the objective lens, reflecting from the surface of the specimen, and then traveling back to the prism along the same route, the intensity of the reflected light is given by

$$\mathcal{I} = \frac{1}{2}(1 - \cos 2\phi). \quad (2)$$

Here $\mathcal{I} \in [0, 1]$ is the normalized intensity (Shribak, 2013) calculated as

$$\mathcal{I} = \frac{\mathcal{I}_{\text{dic}} - \mathcal{I}_s}{\mathcal{I}_0} \quad (3)$$

where \mathcal{I}_{dic} is the intensity of the DIC image, \mathcal{I}_0 is the reference intensity of the image without DIC and \mathcal{I}_s is the offset intensity caused by the stray light in the absence of the illumination source. In the Eq. (2), ϕ is the optical path difference between E_x and E_y . It consists of two parts

$$\phi = \phi_z + \gamma \quad (4)$$

where $\phi_z = \frac{2\pi}{\lambda} [[z]]$ is the phase change due to the local surface height jump $[[z]]$, and γ is the retarded phase from E_x to E_y caused by the Nomarski prism. λ is the wavelength of the incident light depending on the illumination source. The

phase lag γ is treated as a bias, which can be tuned by adjusting the position of the prism along x -axis. This bias is an important instrumental parameter used as (1) an indicator for the sign of the surface height gradient; (2) an accommodator for achieving the optimal phase contrast. We will discuss these later.

Let $\mathbf{s} = (s_x, s_y)$ be the beam-shear vector. In general, $s_x = s = f\epsilon$ and $s_y = 0$ for all commercial DIC microscopes, by which we can only characterize the surface height variation along x -axis. As mentioned earlier, the martensitic materials have an important feature that the surface distorts during the phase transformation corresponding to the finite piecewise linear deformations, which are characterized by the symmetry-related transformation stretch tensors (Ball and James, 1987; Chen et al., 2013; Song et al., 2013). We can use a piecewise linear function $z = z(x)$ to represent the surface topography of martensite structures, e.g. the zigzags as shown in Fig. 2(b) characterized by

$$z(x) = \begin{cases} 0, & x < x_i - w_1; \\ \tan\theta(x - x_i + w_1), & \text{or } x \geq x_i + w_2; \\ -\frac{w_1}{w_2} \tan\theta(x - x_i - w_2), & x_i - w_1 \leq x < x_i; \\ & x_i \leq x < x_i + w_2. \end{cases} \quad (5)$$

The positions $x_i - w_1$, x_i and $x_i + w_2$ indicate the interfaces at which the surface gradient jumps. $w_1 > 0$ and $w_2 > 0$ characterize the domain sizes corresponding to the non-zero surface gradients. θ is the surface angle associated with the domain $[x_i - w_1, x_i]$ corresponding to the surface gradient $\tan\theta$. For $s < \min(w_1, w_2)$, the DIC microscope measures $[[z]] = z(x + s) - z(x)$ that exactly equals to $s\nabla z$ for $x \in [x_i - w_1, x_i - s] \cup [x_i, x_i + w_2 - s]$. In the regions of $[x_i - w_1 - s, x_i - w_1]$, $[x_i - s, x_i]$ and $[x_i + w_2 - s, x_i + w_2]$, the DIC measures are uncertain. The accuracy depends on the beam-shear distance s . As $s \rightarrow 0$, the size of uncertain domain vanishes. The analytic gradient and the DIC measure are compared in Fig. 2(c) for various topographies at $s = \frac{w_1}{5}$. Assume that the fineness of microstructure is larger than the beam-shear distance along the beam splitting direction under the DIC microscope, the measure of $[[z]]$ can be used to approximate the local surface gradient. According to the assumption that the surface topography is piecewise linear, $\nabla z(\frac{x}{\lambda}) = \nabla z(x)$, we can rewrite the Eq. (2) as

$$\hat{I} \approx \frac{1}{2} [1 - \cos 2(2\pi\hat{s}\nabla z + \gamma)] \quad (6)$$

for the relative beam-shear distance $\hat{s} = \frac{s}{\lambda}$. The approximately equal sign becomes exact at relative positions $\frac{\hat{s}}{2}$ away from the interface. Suppose that an interface between martensite variants is atomically sharp, for a given illumination source, the observed width of the interface of a DIC image implies the beam-shear distance of the microscope. In other words, the DIC microscope with a smaller beam-shear distance resolves the interface better. In principle, we can manipulate the orientation between the incident rays and the birefringence axes of the prism to minimize the beam-shear angle so as to improve the DIC resolution for interface.

The equation (6) is a periodic function of ∇z with periodicity $\frac{1}{2\hat{s}}$. Within one period, there exist two solutions for

$$(\nabla z)^\pm = \frac{1}{2\pi\hat{s}} \left(-\gamma \pm \frac{1}{2} \arccos(1 - 2I) \right). \quad (7)$$

Since the surface gradient is independent of bias, the differentiation of Eq. (7) with respect to bias γ gives

$$\left(\frac{\partial I}{\partial \gamma} \right)^\pm = \pm 2\sqrt{I - I^2}. \quad (8)$$

Eq. (8) suggests that if the DIC microscope starts at bias $\gamma = 0$, the intensity increases as the increasing of bias for the positive surface gradient, vice versa. This is illustrated in Fig. 3. It plots the variation of intensity as a function of the surface angle $\theta = \arctan(\nabla z)$. The maximum angular range of the surface that can be uniquely determined by Eq. (6) is $[-\arctan(\frac{1}{4\hat{s}}), \arctan(\frac{1}{4\hat{s}})]$ labeled as the gray dashed lines. As an example shown in Fig. 3, we choose $\hat{s} = 0.4$ corresponding to the measurable angular range from -32° to 32° . Within this range, the intensity is zero when surface is completely flat at bias 0, and increases as the surface starts tilting. As indicated by the black arrow in Fig. 3, the intensity increases with slight increasing of bias for the positive branch of surface angles. When the surface angle $|\theta| > \arctan(\frac{1}{4\hat{s}})$, the determination of the sign of surface gradient by Eq. (8) will fail. Reducing the relative beam-shear distance will expand the range of measurable surface gradient.

We simulate the intensity for the surface topography defined in Eq. (5) with the dimensionless geometric parameters $\hat{s} = 0.4$, $x_i = 2.5$, $w_1 = 2$, $w_2 = 5$ at various surface angles θ in the range of $[-32^\circ, 32^\circ]$ in Fig. 4. This suggests that the surface height gradient along the beam-shear direction is readily computed by the Eq. (7) from the intensity values of the DIC image. If there exists a jump of the gradient along the beam-shear direction, the intensity suddenly drops to zero, and the measured width of such discontinuity equals the relative beam-shear $|\hat{s}|$.

3. Calibration of the optical parameters

In order to quantitatively calculate the surface gradient through Eqs. (7) and (8), we need to calibrate the stray light intensity \mathcal{I}_s of the whole optical system, as well as the bias γ and the relative beam-shear \hat{s} of the DIC module. These values are not provided by commercial microscopes. First, \mathcal{I}_s is calibrated together with the calibration of the origin of the

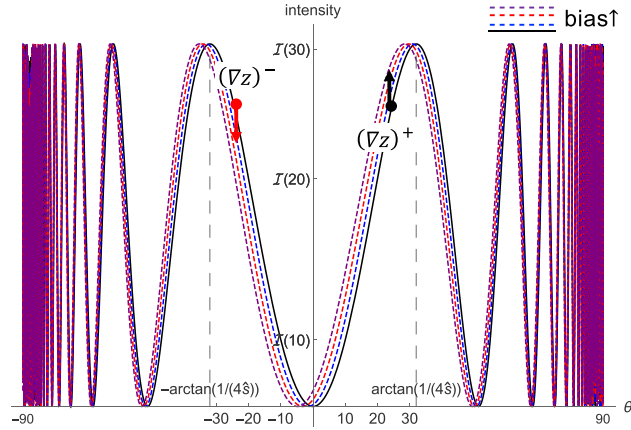


Fig. 3. The intensity as a function of the surface angle between -90° and 90° at different bias. The dimensionless relative beam-shear distance \hat{s} is chosen as 0.4.

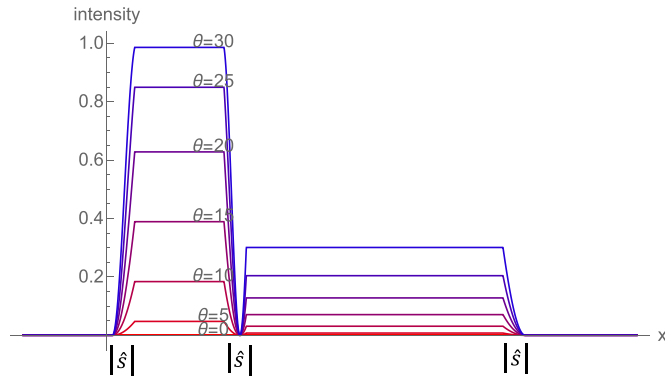


Fig. 4. The intensity as a function of position for the surface topography given by Eq. (5) at the surface angles $0^\circ, 5^\circ, 10^\circ, 15^\circ, 20^\circ, 25^\circ$ and 30° of the left level in $[x_i - w_1, x_i]$.

bias using a standard 6 inch silicon wafer. We assume its surface is flat. By Eqs. (2) and (3), we get the normalized DIC intensity

$$\hat{I}_{\text{dic}} = \frac{1}{2} \sin^2 \gamma + \hat{I}_s, \tag{9}$$

for

$$\hat{I}_{\text{dic}} = \frac{I_{\text{dic}}}{I_0}, \text{ and } \hat{I}_s = \frac{I_s}{I_0}.$$

The first and second terms of Eq. (9) are both non-negative. We monitor the intensity of the image of the flat region as continuously tuning the bias knob of the DIC module. The minimum intensity of the flat region tells the position of zero bias of the DIC, while the corresponding intensity value gives the stray light intensity I_s by Eq. (9). Fig. 5(a) shows the DIC image of the surface of the silicon wafer. Along the beam-shear direction, we plot the normalized intensity for the bias corresponding to the minimum intensity of flat region. As shown in red of Fig. 5(b), the stray light intensity $I_s \approx 0.26$. We mark the position of the zero bias on the knob for reference.

To calibrate the positive direction of the bias, we engraved a sharp surface step on top of the silicon wafer by the standard lithography process. The step profile was characterized by the atomic force microscope as shown in Fig. 5(a). The step of height 79nm results in a peak in the intensity spectrum along the beam-shear direction. We monitor the intensity of the peak while slightly turn the bias knob clockwise. In this case, the clockwise tuning reduces the intensity of the peak with respect to the reference, exhibited as the left peak of the blue spectrum in Fig. 5(b). From the AFM result, we confirm that this step is going downwards along the beam-shear direction. By Eq. (8), the clockwise direction of the knob of DIC module defines the positive direction of the bias.

Finally, the relative beam-shear \hat{s} is calibrated by the martensite microstructure of CuAlNi. The specimen was provided by the research group of the University of Minnesota (see their publications (Abeyaratne et al., 1995; Chu, 1993) for details of the specimen). The nominal composition of the specimen is Cu-14 wt%Al-3.9 wt% that undergoes cubic to orthorhombic transformation during cooling at $\sim 30^\circ\text{C}$ with a large thermal hysteresis of $\sim 20^\circ\text{C}$. The topographic parameters of a

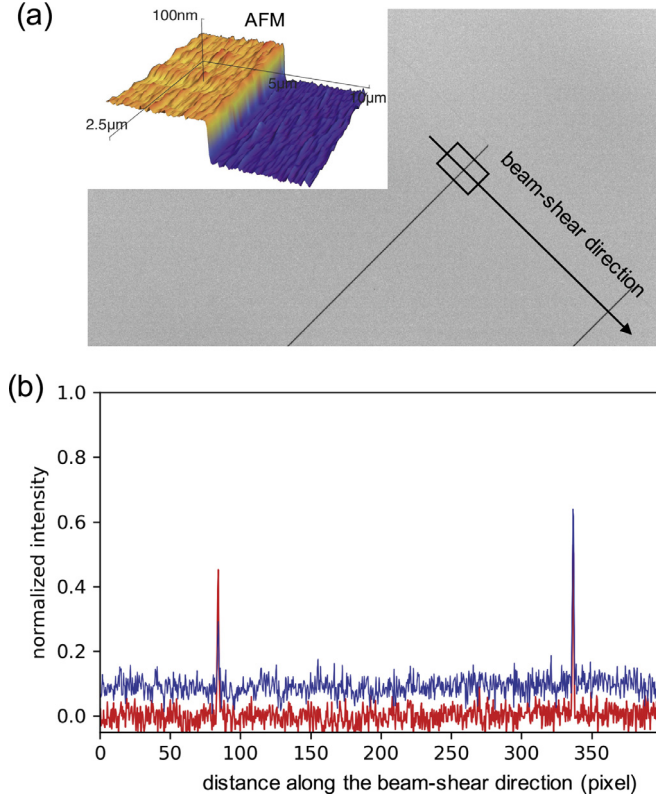


Fig. 5. (a) DIC image of the flat surface of a standard 6 in. silicon wafer at the bias tuned to be zero. The up left inset is the AFM image of the silicon wafer with a surface step. (b) The intensity of the DIC image along the beam-shear direction for bias 0 (red) and 0⁺ (blue). (For interpretation of the references to colour in this figure legend, the reader is referred to the web version of this article.)

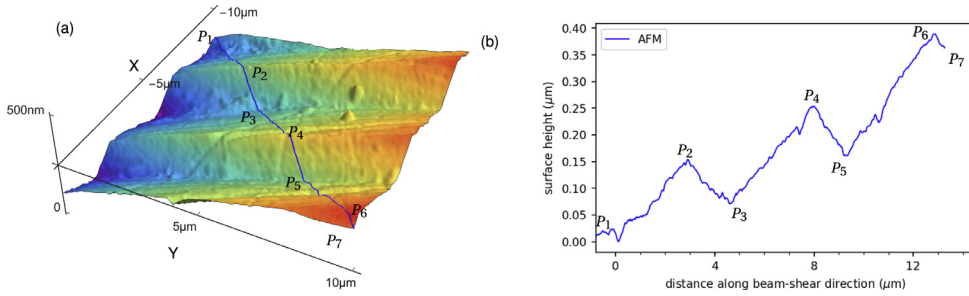


Fig. 6. (a) The surface topography of the region in martensite CuAlNi characterized by the atomic force microscope. (b) Surface height profile given by AFM along the beam-shear direction of DIC. (For interpretation of the references to color in this figure legend, the reader is referred to the web version of this article.)

twin sequence were characterized by the atomic force microscope (AFM) as shown in Fig. 6. The zig-zag line labeled by vertices $\{P_i\}$ where $i = 1, 2, \dots, 7$ corresponds to the beam-shear direction of our DIC microscope. As plotted in Fig. 6(b), it is piecewise linear, which can be interpreted by the function

$$z_P(x) = \begin{cases} K_j^+(x - P_{2j-1}) + z_P(P_{2j-1}), & \text{for } P_{2j-1} \leq x < P_{2j} \\ K_j^-(x - P_{2j}) + z_P(P_{2j}), & \text{for } P_{2j} \leq x < P_{2j+1}. \end{cases} \quad (10)$$

Here, the parameters K_j^+ , K_j^- , $j = 1, 2, 3$ are the positive/negative slopes of the linear functions corresponding to the data between the point P_{2j-1} and P_{2j+1} . The data segment $[P_3, P_5]$ used as the reference for the calibration of \hat{s} . The positive and negative slopes of this segment were fitted by (10). The mean values of K_2^+ and K_2^- are calculated as 0.05046 ± 0.00086 and -0.0643 ± 0.0029 respectively, by which we use the Eq. (7) at bias $\gamma = 0$ to compute the parameter $\hat{s}^+ = 2.3599$ and $\hat{s}^- = 2.2883$. We take the average of \hat{s}^\pm as the representation for the relative beam-shear $\hat{s} = 2.3241$ used in our experiment.

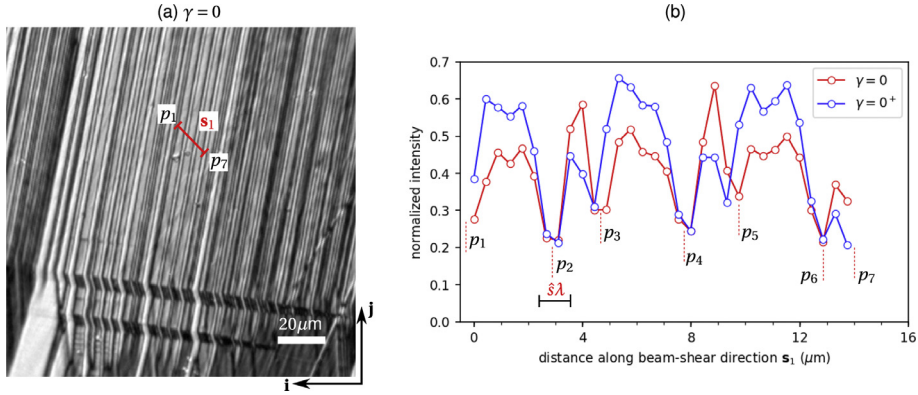


Fig. 7. (a) The normalized DIC image of the twinned martensite microstructure of CuAlNi specimen. (b) The normalized intensity along the beam-shear direction corresponding to the region scanned by the atomic force microscopy.

4. Surface topography measurement by DIC microscope

With the calibrated optical system parameters, we conducted the quantitative surface height gradient measurement. To verify our theoretical model and the proposed approach in section 2, we compared the corresponding region with the AFM result. Note that the area of view under our optical microscope is much larger than the scanned region by AFM. In order to get a good comparison, we aligned the scanning basis $\mathbf{X} - \mathbf{Y}$ (Fig. 6) with the sample basis $\mathbf{i} - \mathbf{j}$ (Fig. 7), and make our DIC micrograph completely cover the region scanned by AFM. The optical beam-shear direction in Fig. 7 is $\mathbf{s}_1 = \mathbf{i} + \mathbf{j}$ in terms of the sample basis in consistent with the blue line depicted in Fig. 6 from vertices P_1 to P_7 . In this section, we will use the upper case letter representing the AFM parameters and the lower case letter representing the DIC parameters.

4.1. Determination of the piecewise gradient of the selected domain

We used the IDS UI-3038CP-C-HQ CMOS camera to acquire the raw images. Integrated with the objective lens, It provides the pixel size $3.45 \mu\text{m} \times 3.45 \mu\text{m}$. Sequentially, we took two DIC images at the bias zero and the bias slightly positive with the Nomarski prism inserted, then took a reference image without the prism. Fig. 7(a) shows the normalized DIC image at $\gamma = 0$ of an area consisting of the laminated twin structure with the average fineness of several microns. The beam-shear direction in our experiment is along the diagonal direction of the image frame. For comparison, we selected the same region from the image along the beam-shear direction of the DIC, i.e. from the point p_1 to the point p_7 marked in Fig. 7(a). The corresponding normalized intensity profiles at the bias $\gamma = 0$ and $\gamma = 0^+$ are shown in Fig. 7(b).

As predicted in previous section, the sensitivity of the intensity with respect to the subtle change of bias reveals the sign of the local surface height gradient along the beam-shear direction. Within the selected region, as slight increasing the bias from zero, the intensity increases in the sub-domains $[p_1, p_2] \cup [p_3, p_4] \cup [p_5, p_6]$, while the intensity decreases in the sub-domains $[p_2, p_3] \cup [p_4, p_5] \cup [p_6, p_7]$. This means that the local slopes are positive in the sub-regions $\cup_{i=1}^3 [p_{2i-1}, p_{2i}]$, and negative in the sub-domains $\cup_{i=1}^3 [p_{2i}, p_{2i+1}]$, which is consistent with the signs of slopes measured by AFM in Fig. 6. The sudden drop of the intensity at each of the vertices p_i implies the width of uncertainty at the interface where the surface gradient jumps. It equals to $\hat{s}\lambda$ where \hat{s} is the relative beam-shear distance defined in Eq. (6) and λ is the wavelength of the light. Roughly, this value tells the characteristic optical shear displacement of the Nomarski prism used for the DIC microscope, although it is not generally provided by the manufacturers. In our experiment, it is approximately $1 \mu\text{m}$. To achieve higher accuracy for such method, we need more precise characterization of the beam-shear distance.

By the Eqs. (7) and (8), we calculated the surface height gradient along the beam-shear direction of the DIC for the selected domain as shown in Fig. 8(a). In order to make a fair comparison with the results characterized by the AFM, we set $z_p(P_1)$ to be the initial value of the analyzed region of the DIC image, i.e. $z(p_1) = z_p(P_1)$. Subjected to this initial condition, we integrated the surface gradient over the domain $[p_1, p_7]$ in the image along the beam-shear direction of the DIC. Fig. 8(b) shows that the surface topography given by the DIC measurement is piecewise linear having the alternating slopes k_i^+ and k_i^- for $i = 1, 2, 3$, which agree well with the measured slopes K_i^+ and K_i^- characterized by the AFM, see table 1. In addition, the characterized interface positions from the DIC method match remarkably well with the AFM results (i.e. the positions of the vertices in Fig. 8(b)).

5. Three-dimensional deformation gradient measurement of a martensite sub-domain

Within a martensitic domain consisting of laminated twin structure, the determination of the local deformations for each of the twin variants plays an important role in understanding the macroscopic mechanical behaviors of the material undergoing the phase transformation. However, this is a non-trivial task because the individual twin lath is at a scale from

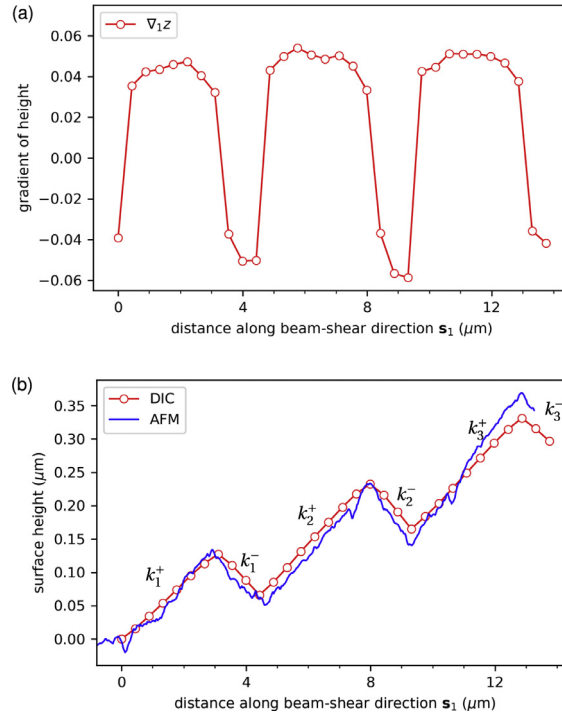


Fig. 8. (a) The calculated surface height gradient along the beam-shear direction marked in the DIC image of Fig. 7(b). The surface topography reconstructed by the DIC measurement, compared with the results given by the atomic force microscope.

Table 1

The slopes of each of the sub-domains in the selected area characterized by AFM and DIC, respectively.

Label of subdomains	Slopes K_i from AFM	Median of slopes k_i from DIC
1 +	0.0558 ± 0.00275	0.0516
1 -	-0.0523 ± 0.00244	-0.0520
2 +	0.05046 ± 0.00086	0.0509
2 -	-0.0643 ± 0.0029	-0.0633
3 +	0.06624 ± 0.00096	0.0513
3 -	-0.0691 ± 0.0043	-0.044

several to tens of microns, while the macroscopic mechanical properties rely on the microstructure as a union of twins, grain boundaries and interfaces at the scale of several millimeters. It requires that the view of the image covers the microstructure of interest while the resolution of the image is beyond the width of the individual twin lath. Clearly, the atomic force probe can not fulfill such a requirement. In this section, we theorize an approach to assign the transformation stretch tensor to each of the specific martensite sub-domains observed by our differential interference contrast microscope, then calculate the three-dimensional local deformation gradients for the laminated twin structure of martensite in CuAlNi.

5.1. Crystallography and mechanics information of single crystal CuAlNi

The set of transformation stretch tensors are determined based on the lattice parameters and symmetries of both austenite and martensite phases,

$$\mathcal{U} = \{\mathbf{Q}\mathbf{U}\mathbf{Q}^T : \mathbf{Q} \in \mathcal{P}^a, \mathbf{U} \in \mathbb{R}_{sym}^{3 \times 3}\} \quad (11)$$

where \mathbf{U} is the transformation stretch tensor (Chen et al., 2016a) that underlies the lattice distortions during the phase transformation, and the set \mathcal{P}^a is the Laue group of the cubic phase (austenite). Using the custom-made temperature gradient stage introduced in reference (Chen et al., 2016b), we conducted the structural characterization for both phases at different temperatures by synchrotron X-ray diffraction (Chen et al., 2016b) at the Beamline 12.3.2 Advanced Light Source, Lawrence Berkeley National Lab. The experiment is divided into two steps: (1) Use the white beam Laue diffraction to characterize the orientation relationships between the lattice basis of austenite and the sample basis $\mathbf{i} - \mathbf{j}$; (2) Use the monochromatic energy scan to get the photon energy at which the interplanar distance of the specific crystallographic plane (hkl) satisfies

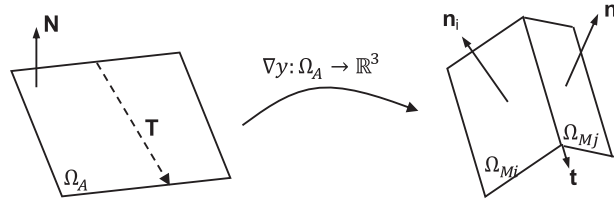


Fig. 9. Kinematics of the homogeneous deformation at the solid-solid phase transformation.

the Bragg diffraction condition. By the first experiment, we get the following parallelism:

$$\mathbf{i} \quad \parallel \left[\begin{array}{ccc} 0.97503 & 0.15493 & 0.15912 \end{array} \right]_c, \quad (12a)$$

$$\mathbf{j} \quad \parallel \left[\begin{array}{ccc} -0.19776 & 0.93171 & 0.30464 \end{array} \right]_c, \quad (12b)$$

$$\mathbf{i} \wedge \mathbf{j} \quad \parallel \left[\begin{array}{ccc} -0.10106 & -0.32849 & 0.93908 \end{array} \right]_c, \quad (12c)$$

where the subscript “c” denotes the vector components written in the cubic basis of austenite. By the second experiment, a set of photon energies for the sufficiently many (hkl) planes is characterized and the lattice parameters are refined for the space group $Fm\bar{3}m$ (austenite) and $Pmmn$ (martensite). The lattice parameters are determined as $a_0 = 5.8391\text{\AA}$ for austenite, and $a = 4.3821\text{\AA}$, $b = 5.3653\text{\AA}$, $c = 4.2133\text{\AA}$ for martensite. By the StrucTrans algorithm (Chen et al., 2016a) we calculated the stretch tensor \mathbf{U} whose ordered eigenvalues are $\lambda_1 < \lambda_2 < \lambda_3$ where $\lambda_1 = 0.91885$, $\lambda_2 = 1.02045$ and $\lambda_3 = 1.0613$. By symmetry relation given in Eq. (11), there are six distinct variants of \mathbf{U} (including \mathbf{U}). They are

$$\begin{aligned} \mathbf{U}_1 &= \begin{bmatrix} \lambda_1 & 0 & 0 \\ 0 & \frac{\lambda_2 + \lambda_3}{2} & \frac{-\lambda_2 + \lambda_3}{2} \\ 0 & \frac{-\lambda_2 + \lambda_3}{2} & \frac{\lambda_2 + \lambda_3}{2} \end{bmatrix}, & \mathbf{U}_2 &= \begin{bmatrix} \lambda_1 & 0 & 0 \\ 0 & \frac{\lambda_2 + \lambda_3}{2} & \frac{\lambda_2 - \lambda_3}{2} \\ 0 & \frac{\lambda_2 - \lambda_3}{2} & \frac{\lambda_2 + \lambda_3}{2} \end{bmatrix}, \\ \mathbf{U}_3 &= \begin{bmatrix} \frac{\lambda_2 + \lambda_3}{2} & 0 & \frac{-\lambda_2 + \lambda_3}{2} \\ 0 & \lambda_1 & 0 \\ \frac{-\lambda_2 + \lambda_3}{2} & 0 & \frac{\lambda_2 + \lambda_3}{2} \end{bmatrix}, & \mathbf{U}_4 &= \begin{bmatrix} \frac{\lambda_2 + \lambda_3}{2} & 0 & \frac{\lambda_2 - \lambda_3}{2} \\ 0 & \lambda_1 & 0 \\ \frac{\lambda_2 - \lambda_3}{2} & 0 & \frac{\lambda_2 + \lambda_3}{2} \end{bmatrix}, \\ \mathbf{U}_5 &= \begin{bmatrix} \frac{\lambda_2 + \lambda_3}{2} & \frac{-\lambda_2 + \lambda_3}{2} & 0 \\ \frac{-\lambda_2 + \lambda_3}{2} & \frac{\lambda_2 + \lambda_3}{2} & 0 \\ 0 & 0 & \lambda_1 \end{bmatrix}, & \mathbf{U}_6 &= \begin{bmatrix} \frac{\lambda_2 + \lambda_3}{2} & \frac{\lambda_2 - \lambda_3}{2} & 0 \\ \frac{\lambda_2 - \lambda_3}{2} & \frac{\lambda_2 + \lambda_3}{2} & 0 \\ 0 & 0 & \lambda_1 \end{bmatrix}. \end{aligned} \quad (13)$$

These six martensite variants form three pairs of compound twins, i.e. (1, 2), (3, 4), (5, 6) and twelve pairs of type I/II twins, i.e. (1, 3), (1, 4), (1, 5), (1, 6), (2, 3), (2, 4), (2, 5), (2, 6), (3, 5), (3, 6), (4, 5), (4, 6). Among these twins, there are 96 austenite-martensite interfaces are possible due to the conditions of compatibility (Ball and James, 1987; Chu, 1993). In order to get relatively simple microstructure, i.e. the laminated twin martensite structure, we designed and fabricated a uniaxial loading device, which applies slight tension to the single crystal specimen along certain crystallographic direction during cooling. Then we got the laminated twin structure shown in Fig. 7(a).

5.2. Kinematics of the deformation

Consider a homogeneous deformation $\nabla \mathbf{y} : \Omega_A \rightarrow \mathbb{R}^3$ that maps the perfectly flat continuous domain in austenite to the twinned martensite characterized by a pair of variants (i, j) for $\mathbf{U}_i, \mathbf{U}_j \in \mathcal{U}$ in (11). For the cubic to orthorhombic phase transformation in CuAlNi , the possible variant pairs (i, j) are either Type I or Type II twins due to the conditions of compatibility (Ball and James, 1987; Chu, 1993) as discussed in the Section 5.1. As illustrated in Fig. 9, let $\mathbf{n}_i = \mathbf{R}\mathbf{U}_i\mathbf{N}$, $\mathbf{n}_j = \mathbf{R}(\mathbf{U}_j + \mathbf{a} \otimes \hat{\mathbf{n}})\mathbf{N}$, where $\mathbf{R} \in \text{SO}(3)$. The vector \mathbf{N} denotes the surface normal vector with $\|\mathbf{N}\| = 1$. The parameters $\mathbf{a}, \hat{\mathbf{n}} \in \mathbb{R}^3$ are the twin shear vector and the normal vector of the twinning plane given by the twin relation

$$\mathbf{Q}\mathbf{U}_j - \mathbf{U}_i = \mathbf{a} \otimes \hat{\mathbf{n}}, \text{ for some } \mathbf{Q} \in \text{SO}(3). \quad (14)$$

There exist and only exist two solutions for the Eq. (14), i.e. $(\mathbf{Q}_I, \mathbf{a}_I, \hat{\mathbf{n}}_I)$ for Type I twin and $(\mathbf{Q}_{II}, \mathbf{a}_{II}, \hat{\mathbf{n}}_{II})$ for Type II twin for the variant pair (i, j) in the set \mathcal{U} . Without loss of generality, we drop the subscript I and II , and express the deformation raised by the variant j as $\mathbf{U}_j + \mathbf{a} \otimes \hat{\mathbf{n}}$. As shown in Fig. 9(a), there exist a vector \mathbf{T} in reference configuration Ω_A , across which each of the sides are deformed by the deformation gradients $\mathbf{R}\mathbf{U}_i$ and $\mathbf{R}(\mathbf{U}_j + \mathbf{a} \otimes \hat{\mathbf{n}})$ such that the subdomains Ω_{Mi} and Ω_{Mj} are compatible with austenite (in a weak sense) through the relation

$$\mathbf{R}(\mathbf{U}_j + \mathbf{a} \otimes \hat{\mathbf{n}}) = \mathbf{I} + \mathbf{b} \otimes \mathbf{m} \quad (15)$$

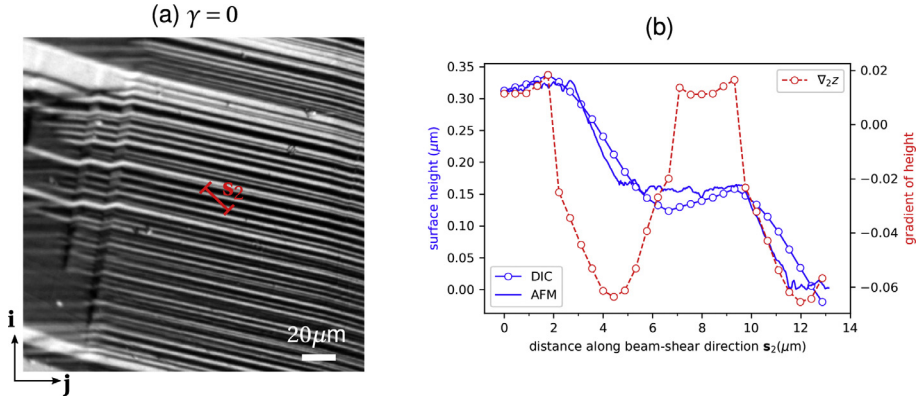


Fig. 10. (a) The DIC image of the 90° in-plane rotated martensite sub-domains. (b) Comparison of the surface topography along the shear direction \mathbf{s}_2 between the AFM and DIC.

for some vectors \mathbf{b} and $\mathbf{m} \in \mathbb{R}^3$ Ball and James (1987). Physically, the vector \mathbf{m} is the austenite/twinned martensite interface normal, and the scalar $f \in [0, 1]$ represents the twinning volume fraction of the lath domain Ω_{Mi} . The deformed configuration of the trace vector \mathbf{T} is calculated as

$$\mathbf{t}(\mathbf{U}_i) = \mathbf{R}[\mathbf{U}_i \mathbf{N} \wedge (\mathbf{U}_i + \mathbf{a} \otimes \hat{\mathbf{n}}) \mathbf{N}] \text{ for } \mathbf{U}_i \in \mathcal{U}. \quad (16)$$

Here the rotation matrix \mathbf{R} solves the Eq. (15). By our DIC measurement, we can determine the deformed configuration of the trace vector \mathbf{t}_{meas} . Therefore, the variant in the region Ω_{Mi} should be

$$\mathbf{U}^* = \arg \min_{\mathbf{U}_i \in \mathcal{U}} \|\mathbf{t}_{\text{meas}} - \mathbf{t}(\mathbf{U}_i)\|. \quad (17)$$

5.3. 3D surface height gradient measurement by DIC

In order to demonstrate our variant assignment approach for the martensitic microstructure using the DIC microscope, we repeat the experiment discussed in section 4.1 along two orthogonal directions, i.e. the direction \mathbf{s}_1 in Fig. 7(a), and the direction \mathbf{s}_2 shown in Fig. 10(a). Note that \mathbf{s}_1 and \mathbf{s}_2 are linearly independent vectors attached to the sample. One is 90° in-plane rotated from the other. The optical calibration parameters such as the relative beam shear \hat{s} and the bias γ remain the same for both measurements. The Fig. 10(b) shows the height gradient for the same martensite sub-domains along $\mathbf{s}_2 = -\mathbf{i} + \mathbf{j}$. The normalized DIC images of Figs. 7(a) and 10(a) give the surface height gradient fields $\nabla_1 z(x, y)$ and $\nabla_2 z(x, y)$ along \mathbf{s}_1 and \mathbf{s}_2 . By direct integration after correlating the two gradient fields within the selected area that matches the region scanned by AFM, we reconstruct the 3-dimensional surface topography in Fig. 11. Though the reconstructed surface area is slight larger than the domains scanned by the AFM, the topography is quite consistent with the twinning geometries of the martensite measured by the AFM.

5.4. Determination of deformation gradients of the martensitic sub-domains

Let the undeformed the surface outer normal vector $\mathbf{N} = -(\mathbf{i} \wedge \mathbf{j})_c$, optical beam-shear vectors $\mathbf{s}_1 = (\mathbf{i} + \mathbf{j})_c$ and $\mathbf{s}_2 = (-\mathbf{i} + \mathbf{j})_c$ in terms of cubic basis given by (12) with norms: $\|\mathbf{N}\| = 1$, $\|\mathbf{s}_1\| = \|\mathbf{s}_2\| = \sqrt{2}$. In Fig. 11(b), for a local point α in the subdomain M_i , the surface relief vectors \mathbf{u}_1 and \mathbf{u}_2 are determined as

$$\mathbf{u}_i(\alpha) = \frac{\nabla_i z(\alpha) \mathbf{s}_i}{\sqrt{2}} + \mathbf{N}, \text{ no sum on } i, \text{ for } i = 1, 2. \quad (18)$$

The local surface normal vector $\mathbf{n}_\alpha = \mathbf{u}_2(\alpha) \wedge \mathbf{u}_1(\alpha)$. The tangential vector of the interface between the neighboring variants is calculated as

$$\mathbf{t}_{\text{meas}} = \pm \mathbf{n}_\alpha \wedge \mathbf{n}_\beta, \text{ for } \alpha \in \Omega_{Mi} \text{ and } \beta \in \Omega_{Mj}. \quad (19)$$

Substituting (19) into (17) and aggregating all twin variants of cubic to orthorhombic transformation listed in (13), we find the pair of variants (2, 5) is the minimizer that represents the deformation of the twin domain labeled in Fig. 11(b). The

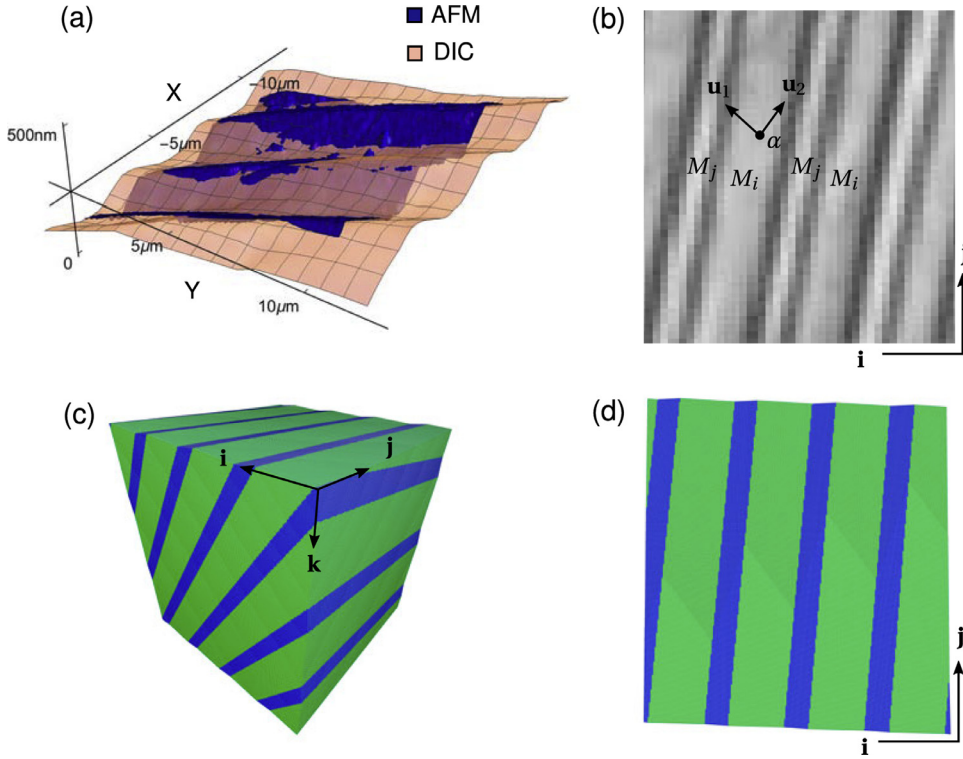


Fig. 11. (a) The surface topography reconstructed by combining the surface gradients along \mathbf{s}_1 and \mathbf{s}_2 for the region (b) in normalized DIC image. (c) Calculated full-field deformation of the martensite with the surface relief in (d).

corresponding solutions of the twin relation in (14) and the crystallographic Eq. (15) are

$$\left\{ \begin{array}{l} \mathbf{R} = \begin{bmatrix} 0.9990 & -0.0401 & -0.0174 \\ 0.0400 & 0.9992 & -0.0053 \\ 0.0176 & 0.0046 & 0.9998 \end{bmatrix} \\ \mathbf{m} = (-0.7547, -0.6201, 0.2144), \\ \mathbf{b} = (0.0668, -0.0648, 0.0252), \\ \mathbf{a} = (0.1605, 0.0542, -0.1828), \\ \hat{\mathbf{n}} = \frac{1}{\sqrt{2}}(1, 0, 1), \end{array} \right. \quad (20)$$

for the twinning volume fraction 27%. By the above solutions, we calculated the three-dimensional deformation of the selected domain corresponding to the DIC measurement. The results shown in Fig. 11(c) and (d) agree with the observation of the surface morphology very well.

6. Further discussion and conclusion

Admittedly, the DIC microscope has been widely used to observe the martensitic microstructures over several decades, almost as old as the shape memory alloys (Abeyaratne et al., 1995; Bhattacharya, 2003; Chen et al., 2016b; Chu, 1993; Cui et al., 2006; Heczko et al., 2013; Song et al., 2013). Thanks to the phase contrast, the surface reliefs of martensite variants are resolved very well and the twin interfaces look very sharp. Unfortunately, this technique was only applied to microstructure observation without any quantitative characterization. The reason is that many optical parameters such as the characteristics of the Nomarski prism, the wavelength of the illumination source and the phase bias are not well calibrated by the commercial optical microscope. In this paper, our quantitative study of the microstructure of martensite in CuAlNi single crystal pumps the potential of this technique towards much wider applications to the experimental mechanics. However there are still many limitations for the current approach.

First, the illumination source provided by Nikon microscope is incoherent by its nature. Such incoherency adds unavoidable errors to the relative beam-shear distance δ . From the specifications provided by Nikon, we can estimate the spatial resolution as $\frac{\lambda}{2NA} \approx 500$ nm where NA denotes the numerical aperture of the objective lens. Better resolution can be achieved in

future by replacing the illumination source of shorter wavelength and the objective lens with larger NA. Second, we can not directly characterize the optical parameters of the commercial DIC module. The shear angle between the two outgoing rays with orthogonal polarization is one of the most important parameters underlying the correctness of the whole approach. In our current settings, we used a standard sample to characterize it, which yields certain unavoidable errors. Regarding the resolution of the local gradient ∇z , it depends on the beam-shear distance at the focal plane of objective lens. According to Figs. 5b, 7b and 10b, we can roughly estimate the beam-shear distance. For example, in Fig. 5b, the half-height peak width is approximately the beam-shear distance, i.e. about 800 nm. In Figs. 7b and 10b, the width of the region where intensity suddenly drops also corresponds to the beam-shear distance, which is around $1\mu\text{m}$. The accuracy of the slopes within each of the isoorientation zone depends on the sampling rate, that is the number of data points are collected. It shows that we can get two data points in a $2\mu\text{m}$ interval (Fig. 7). By comparing the slopes calculated by DIC with those given by AFM, we can roughly estimate that the accuracy of the slope measurement is about $\text{ArcTan}(0.005) \approx 0.005$ rad. We are working on a more accuracy method to directly determine the beam-shear angle for Nomarski prism. This will assist us to achieve higher precision for the surface deformation measurement in future. Last but not least, the reconstruction of 3D surface topographical measurement by our DIC method requires two sets of images with respect to two independent beam-shear directions. Right now, we need to manually rotate the sample stage relative to the objective lens, and correlate the two sets of images in the post processing procedure. We are developing a dual beam-shear DIC microscope, which can spontaneously take two sets of DIC images for dual directions. By this advanced technique, we will be able to do quantitative characterization of the evolution of microstructure and the corresponding full-field deformation in situ during the phase transformation.

Acknowledgment

Z. Z., C. Z. and X. C. thank the financial support of the HK Research Grants Council under Grant 26200316 and 16201118. S. D. acknowledges supports from Light Innovation Technology Ltd through a research contract with the Hong Kong University of Science and Technology (HKUST) R and D Corporation Ltd (Project code 16171510), and the Offices of the Provost, VPRG and Dean of Science, HKUST (project no. VPRGO12SC02). Advanced Light Source was supported by the Office of Science, Office of Basic Energy Sciences, of the U.S. Department of Energy under Contract no. DE-AC02-05CH11231.

References

- Abeyaratne, R., Chu, C., James, R.D., 1995. Kinetics of materials with wiggly energies: theory and application to the evolution of twinning microstructures in a cu-al-ni shape memory alloy. *Phil. Mag.* A 73 (2), 457–497.
- Ball, J.M., James, R.D., 1987. Fine phase mixtures as minimizers of energy. *Arch. Ration. Mech. Anal.* 100 (1), 13–52.
- Bhattacharya, K., 2003. *Microstructure of Martensite: why it Forms and how it Gives Rise to the Shape-memory Effect*. Oxford series on materials modeling, 2. Oxford University Press.
- Bhatti, K., El-Khatib, S., Srivastava, V., James, R.D., Leighton, C., 2012. Small-angle neutron scattering study of magnetic ordering and inhomogeneity across the martensitic phase transformation in $\text{ni}_{50-x}\text{co}_x\text{mn}_{40}\text{sn}_{10}$ alloys. *Phys. Rev. B* 85, 134450.
- Chen, X., Song, Y., Tamura, N., James, R.D., 2016. Determination of the stretch tensor for structural transformation. *J. Mech. Phys. Solids* 93, 34–43.
- Chen, X., Srivastava, V., Dabade, V., James, R.D., 2013. Study of the cofactor conditions: conditions of supercompatibility between phases. *J. Mech. Phys. Solids* 61, 2566.
- Chen, X., Tamura, N., MacDowell, A., James, R.D., 2016. In-situ characterization of highly reversible phase transformation by synchrotron X-ray laue microdiffraction. *Appl. Phys. Lett.* 108, 211902.
- Chluba, C., Ge, W., Lima de Miranda, R., Strobel, J., Kienle, L., Quandt, E., Wuttig, M., 2015. Ultralow-fatigue shape memory alloy films. *Science* 348 (6238), 1004.
- Chu, C., 1993. *Hysteresis and microstructure: a study of biaxial loading on compound twins of copper-aluminum-nickel single crystals*. the University of Minnesota. Ph.D. thesis.
- Cui, J., Chu, Y.S., Famodu, O.O., Furuya, Y., Hattrick-Simpers, J., James, R.D., Ludwig, A., Thienhaus, S., Wuttig, M., Zhang, Z., Takeuchi, I., 2006. Combinatorial search of thermoelastic shape-memory alloys with extremely small hysteresis width. *Nature Mater.* 5 (4), 286.
- Durelli, A.J., Parks, V.J., 1970. *Moiré analysis of strain*. Prentice Hall.
- de Groot, P., 2015. Principles of interference microscopy for the measurement of surface topography. *Adv. Opt. Photon.* 7 (1), 1–65.
- Heczko, O., Straka, L., Seiner, H., 2013. Different microstructures of mobile twin boundaries in 10 m modulated ni-mn-ga martensite. *Acta Mater.* 61 (2), 622–631.
- James, R.D., Zhang, Z., 2005. A way to search for multiferroic materials with “unlikely” combinations of physical properties. In: Planes, A., Mañosa, L., Saxena, A. (Eds.), *Magnetism and Structure in Functional Materials*. Springer Berlin Heidelberg, pp. 159–175.
- Kimiecik, M., Jones, J.W., Daly, S., 2016. The effect of microstructure on stress-induced martensitic transformation under cyclic loading in the SMA nickel-Titanium. *J. Mech. Phys. Solids* 89, 16.
- Li, Y., Zhao, D., Liu, J., Qian, S., Li, Z., Gan, W., Chen, X., 2018. Energy-Efficient elastocaloric cooling by flexibly and reversibly transferring interface in magnetic shape-memory alloys. *ACS Appl. Mater. Interfaces* 10 (30), 25438–25445.
- Meethong, N., HY, H., Speakman, S.A., Carter, W.C., Chiang, Y.M., 2007. Strain accommodation during phase transformations in olivine-based cathodes as a materials selection criterion for high-power rechargeable batteries. *Adv. Funct. Mater.* 00, 1.
- Ni, X., Greer, J.R., Bhattacharya, K., James, R.D., Chen, X., 2016. Exceptional resilience of small-scale $\text{au}_{30}\text{cu}_{25}\text{zn}_{45}$ under cyclic stress-induced phase transformation. *Nano Lett.* 16 (12), 7621.
- Nomarski, G., 1952. Interferential polarizing device for study of phase object. US Patent 2924142.
- Peters, W., Ranson, W., 1982. Digital imaging techniques in experimental stress analysis. *Opt. Eng.* 21 (3), 213427.
- Shribak, M., 2013. Quantitative orientation-independent DIC microscope with fast switching shear direction and bias modulation. *J. Opt. Soc. Am. A Opt. Image Sci. Vis.* 30 (4), 769.
- Song, Y., Chen, X., Dabade, V., Shield, T.W., James, R.D., 2013. Enhanced reversibility and unusual microstructure of a phase-transforming material. *Nature* 502, 85.
- Srivastava, V., Chen, X., James, R.D., 2010. Hysteresis and unusual magnetic properties in the singular heusler alloy $\text{ni}_{45}\text{co}_5\text{mn}_{40}\text{sn}_{10}$. *Appl. Phys. Lett.* 97 (1), 014101.
- Srivastava, V., Song, Y., Bhatti, K., James, R.D., 2011. The direct conversion of heat to electricity using multiferroic alloys. *Adv. Energy Mater.* 1, 97–104.

- Zarnetta, R., Takahashi, R., Young, M., Savan, A., Fruya, Y., Thienhaus, S., Maaß, B., Rahim, M., Frenzel, J., Brunken, H., Chu, Y.S., Srivastava, V., James, R.D., Takeuchi, I., Eggeler, G., Ludwig, A., 2010. Identification of quaternary shape memory alloys with near-zero thermal hysteresis and unprecedented functional stability. *Adv. Funct. Mater.* 20 (12), 1917–1923.
- Zhang, X., Sun, Q.P., Shouwen, Y., 2000. A non-invariant plane model for the interface in CuAlNi single crystal shape memory alloys. *J. Mech. Phys. Solids* 48 (2163).
- Zhang, Z., James, R.D., Müller, S., 2009. Energy barriers and hysteresis in martensitic phase transformations. *Acta Mater.* 57 (15), 4332–4352.
- Zhao, D., Liu, J., Chen, X., Sun, W., Li, Y., Zhang, M., Shao, Y., Zhang, H., Yan, A., 2017. Giant caloric effect of low-hysteresis metamagnetic shape memory alloys with exceptional cyclic functionality. *Acta Mater.* 133, 217.